Supporting information

Surface in-situ self-reconstructing hierarchical structures derived from ferrous carbonate as efficient bifunctional iron-based catalysts for oxygen and hydrogen evolution reactions

Taotao Gao,[a] Caixia Zhou,[c] Xiaojuan Chen,[b] Zhihan Huang,[b] Hongyan Yuan[b] and Dan Xiao[a, b]*

a Institute for Advanced Study, Chengdu University, Chengdu, 610106, P. R. China

E-mail: xiaodan@scu.edu.cn

b College of Chemical Engineering, Sichuan University, 610064, P. R. China

c Institute of New Energy and Low-Carbon Technology, Sichuan University, 610064, P. R. China

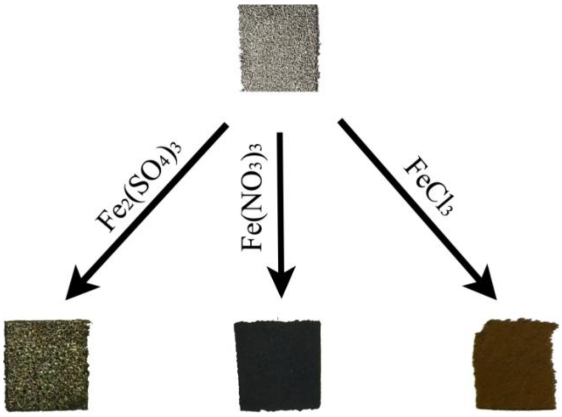

Fig. S1 The colors of the catalytic electrodes based on different iron resources.

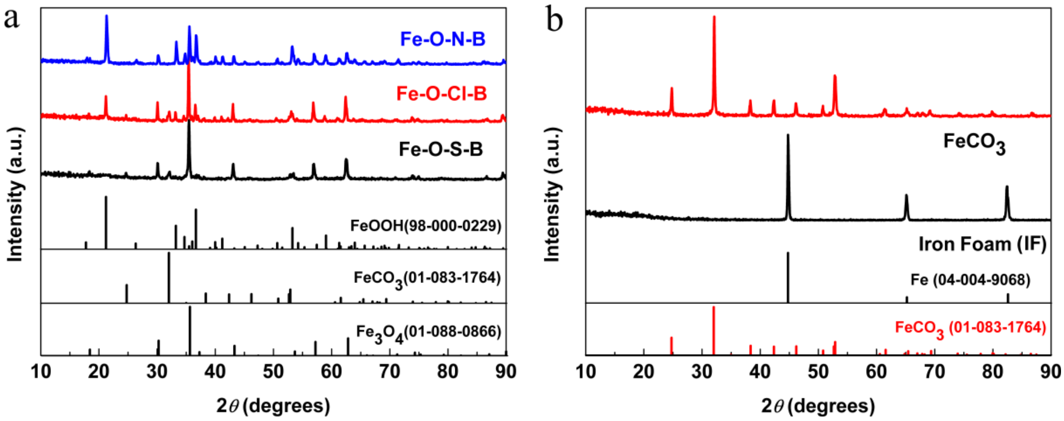

Fig. S2 a) The XRD patterns of Fe-O-S-B, Fe-O-N-B and Fe-O-Cl-B, b) the XRD patterns of $FeCO_3$ powder and IF.

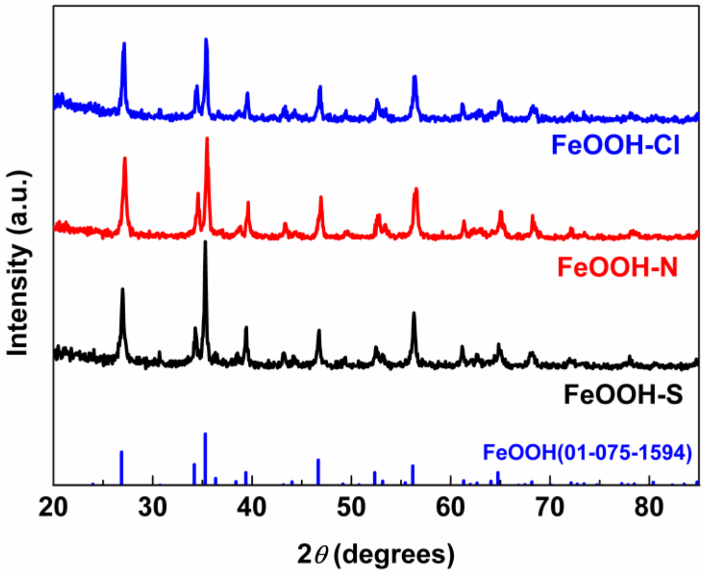

Fig. S3 The XRD patterns of FeOOH-S, FeOOH-N and FeOOH-Cl.

Table S1. The pH of the solutions based on different iron resources.

Iron resource	$Fe(NO_3)_3$	$FeCl_3$	$Fe_2(SO_4)_3$
pH	2.28	2.26	2.15

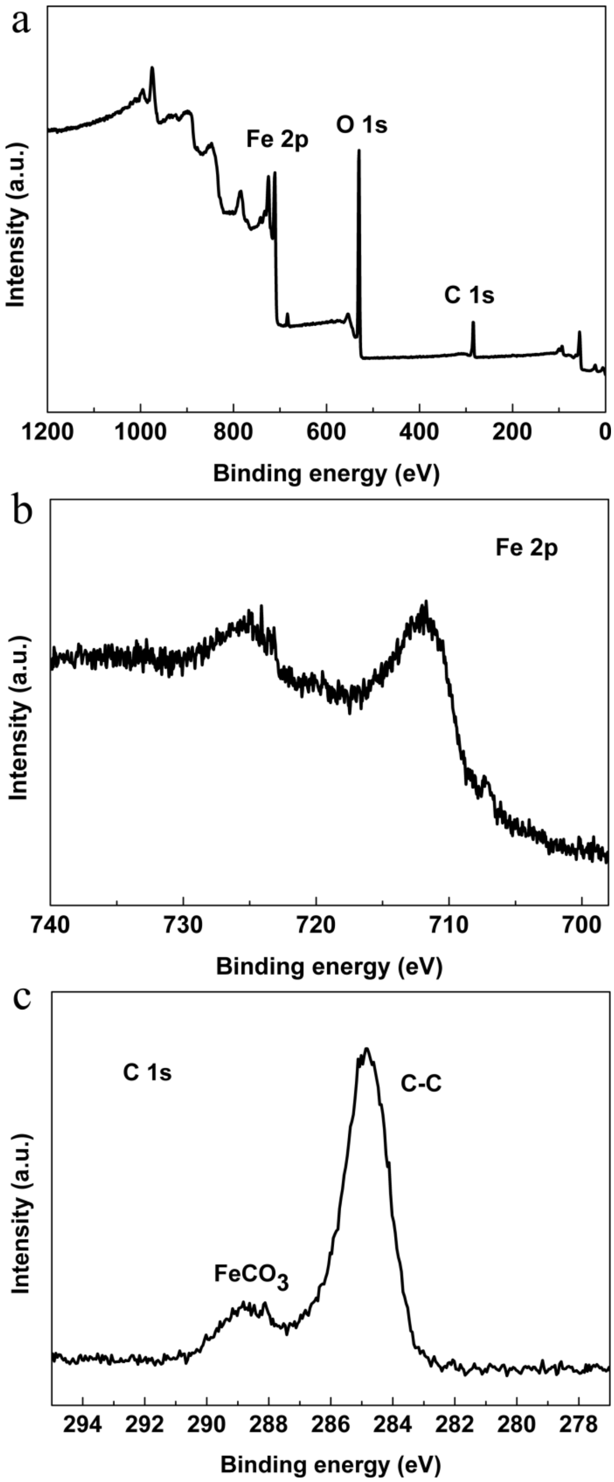

Fig. S4 a) The full XPS spectrum, b) Fe 2p and c) C 1s XPS spectra of $FeCO_3$@IF.

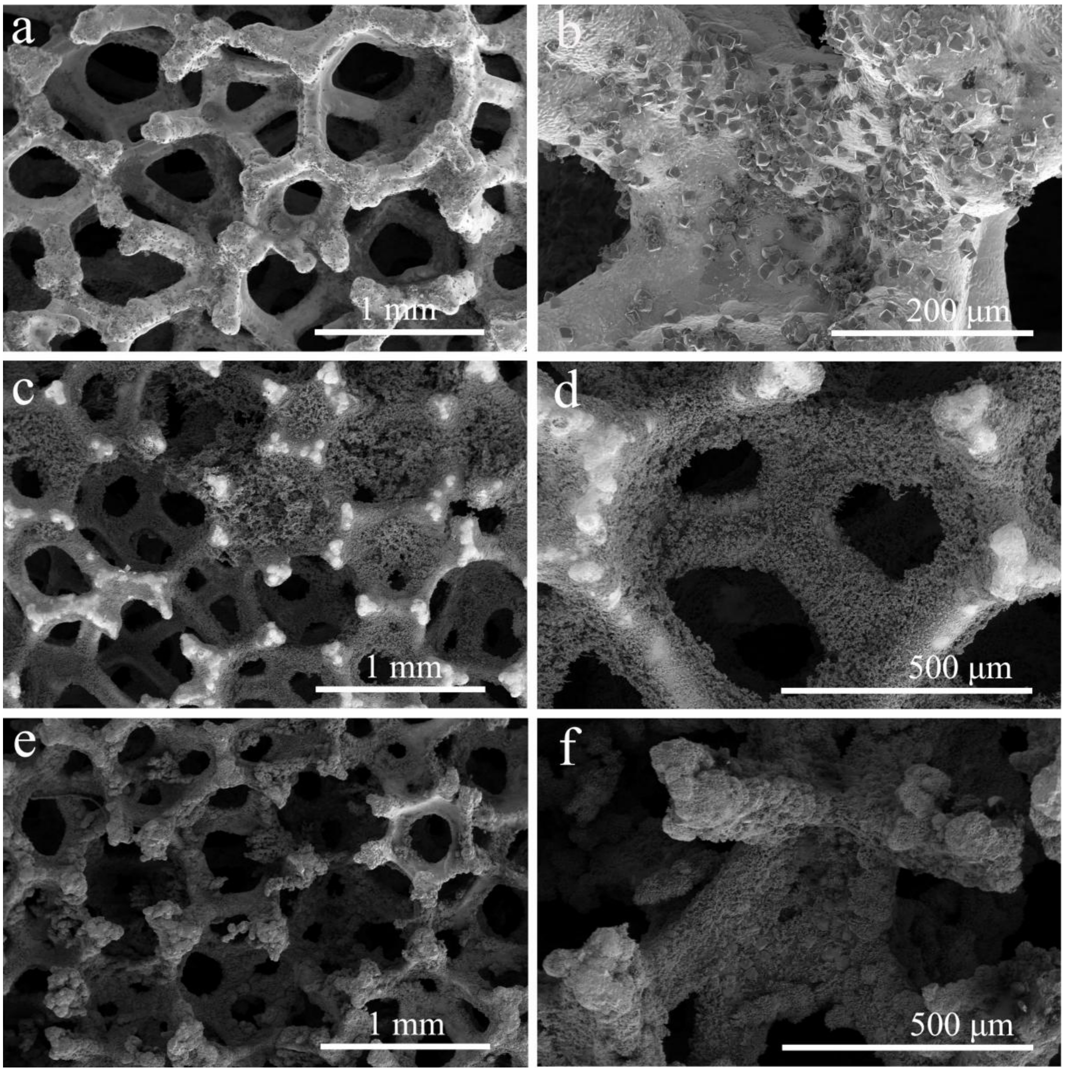

Fig. S5 The SEM images of a, b) $FeCO_3$@IF, c, d) Fe_3O_4@IF and e, f) Fe-O-M@IF.

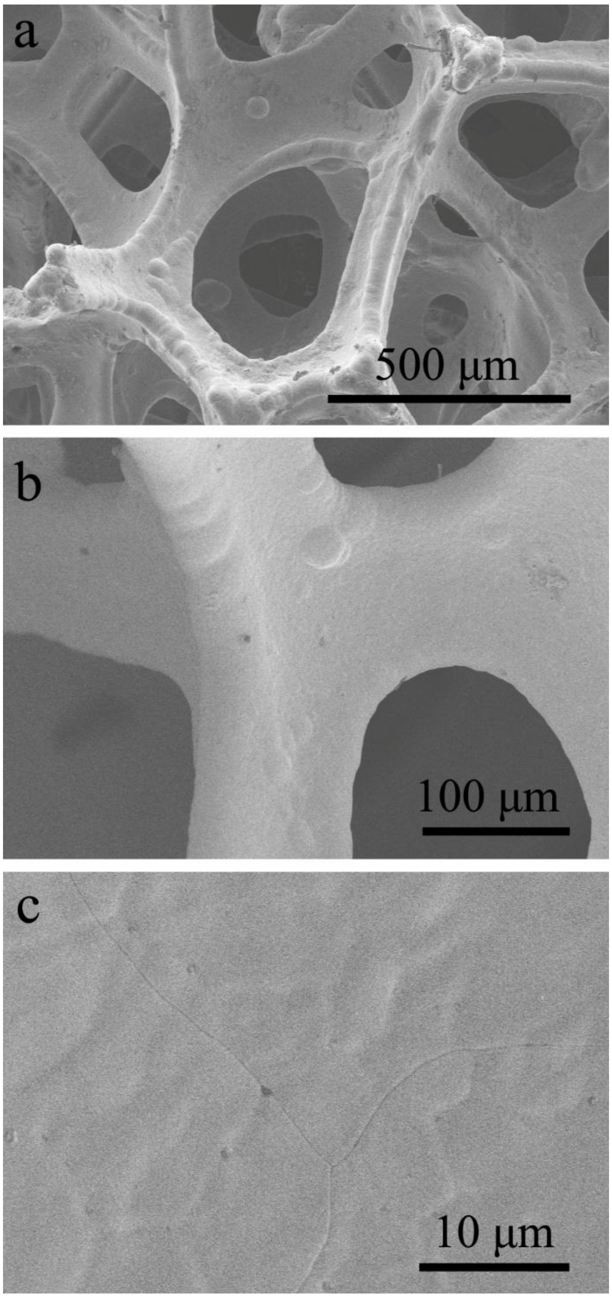

Fig. S6 The SEM images of IF.

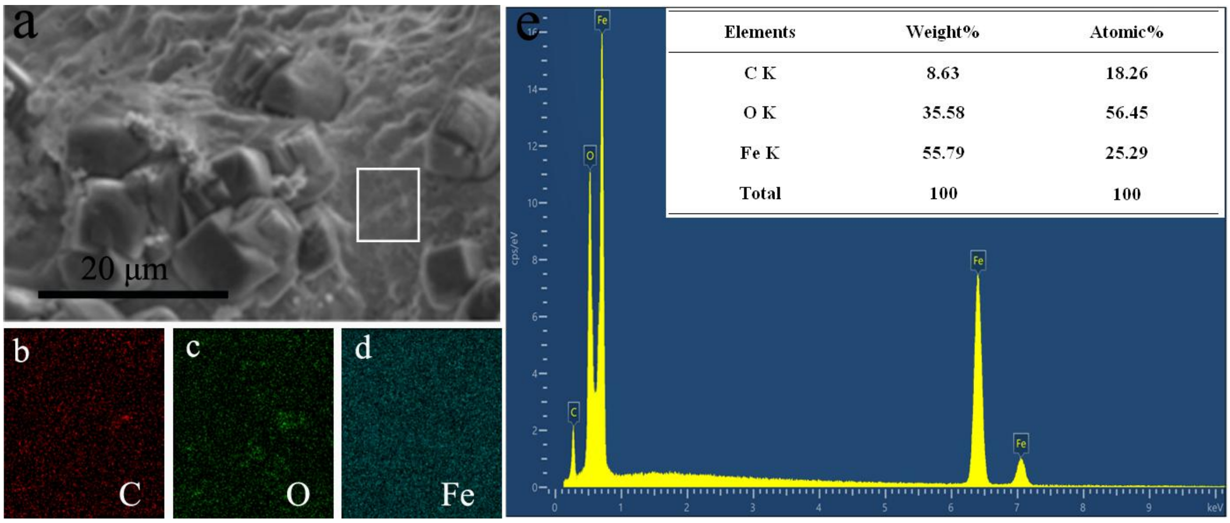

Fig. S7 a) The SEM image of $FeCO_3$@IF, b), c), and d) the distribution of elements (C, O and Fe, respectively), e) the corresponding EDS spectrum.

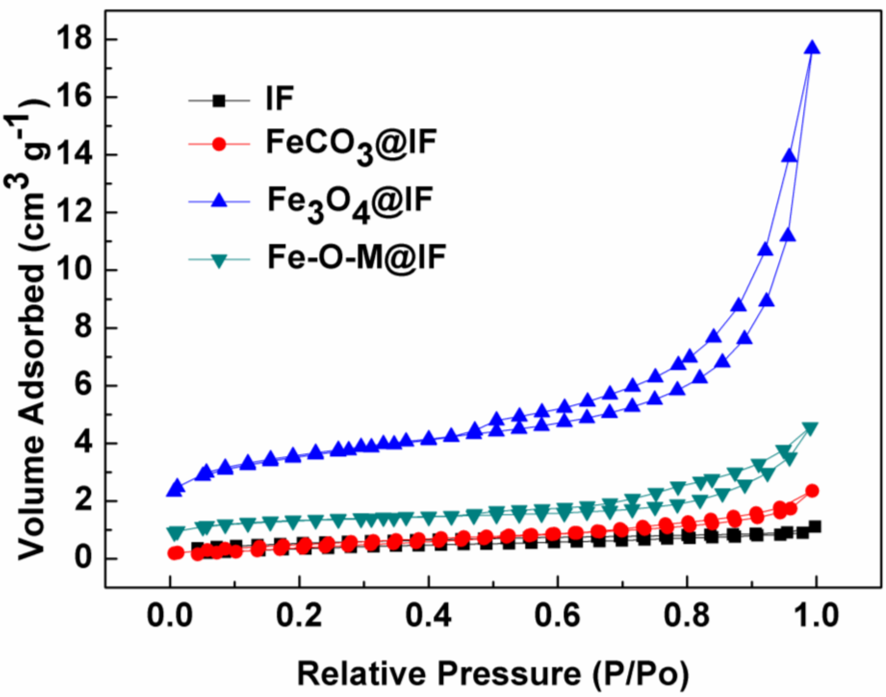

Fig. S8 The N_2 adsorption-desorption isotherm of the electrodes.

Table S2. The specific surface area of IF, $FeCO_3$@IF, Fe_3O_4@IF and Fe-O-M@IF electrodes.

Electrode	IF	$FeCO_3$@IF	Fe_3O_4@IF	Fe-O-M@IF
Specific surface area (m^2 g^{-1})	0.673	1.912	12.690	4.661

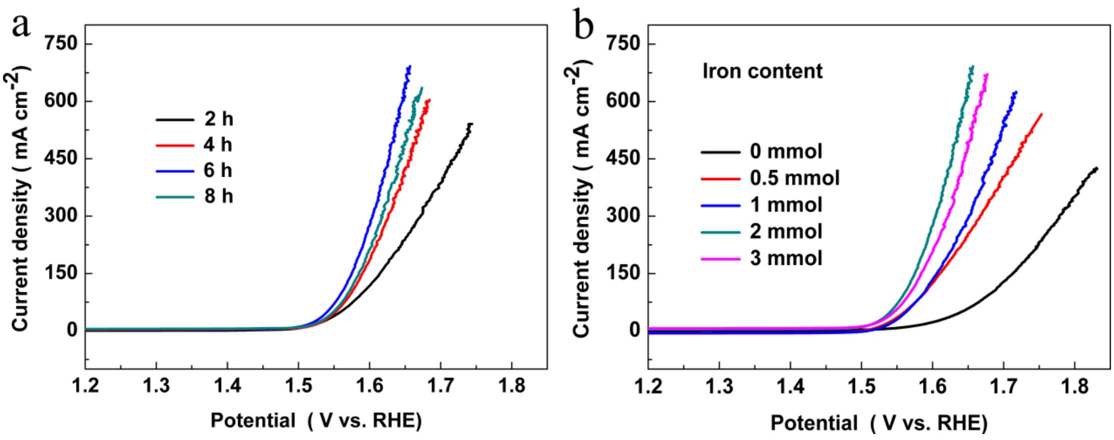

Fig. S9 The polarization curves of the $FeCO_3$@IF electrodes based on different a) hydrothermal reaction time and b) Fe^{3+} content in solution ($Fe_2(SO_4)_3$ as iron resource).

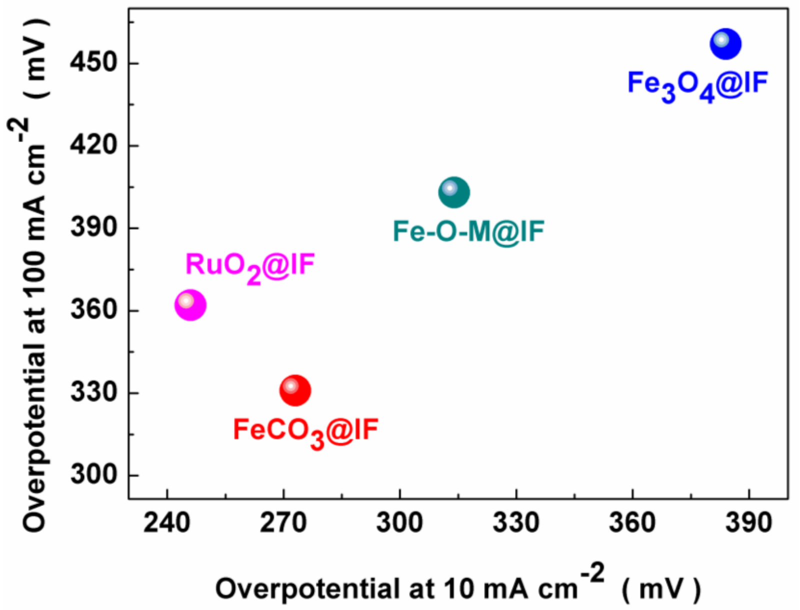

Fig. S10 The overpotential at the current density of 10 and 100 mA cm^{-2} of the catalysts.

Table S3. The comparison of OER catalytic activity in 1 M KOH

Catalysts	Tafel slope (mV dec $^{-1}$)	Overpotential (mV) @ 10 mA cm $^{-2}$	References
FeO_x	93	588	[1]
FeOOH nanoparticles	-	~330	[2]
FeOOH@NF	60	307	[3]
Fe_2O_3/CNT	61	370	[4]
CP@FeP	64	350	[5]
Fe/Fe_3CF@CNT@Fe	49	288	[6]
Co_4N nanowire arrays	44	257	[7]
Np-$(Co_{0.52}Fe_{0.48})_2P$	30	270	[8]
NiCo LDH	40	367	[9]
NiFe-LDH	47	350	[10]
$Ni_{30}Fe_7Co_{20}Ce_{43}O_x$	70	410	[11]
Co-Fe-O@MWCNT	51	368	[12]
Ni/Ni_3N	60	~322	[13]
NiFeP	87	280	[14]
$FeCO_3$@IF	59	273	This work
Fe_3O_4@IF	71	384	This work
Fe-O-M@IF	73	314	This work

Table S4. The comparison of OER catalytic activity of the RuO_2 materials in 1 M KOH

Catalytic electrodes	Tafel slope (mV dec $^{-1}$)	Overpotential (mV) @10 mA cm^{-2} /100 mA cm $^{-2}$	References
RuO_2@Iron foam	87	246/362	This work
RuO_2@ Iron foam	47	～310/-	[15]
RuO_2@ Iron foam	72	～270/～350	[16]
RuO_2@ Ni foam	88	～240/～350	[17]
RuO_2@ Ni foam	66	～300/～380	[18]
RuO_2@ Ni foam	99	～270/～390	[19]
RuO_2@ Ni foam	58	242/～480	[20]
RuO_2@ Carbon cloth	66	～270/～350	[21]
RuO_2@ Carbon cloth	69	295/～390	[22]
RuO_2@ Carbon cloth	103	～210/～340	[23]
RuO_2@ Glassy carbon	93	～340/-	[24]
RuO_2@ Glassy carbon	57	～260/-	[25]
RuO_2@ Co foam	139	～240/～370	[26]

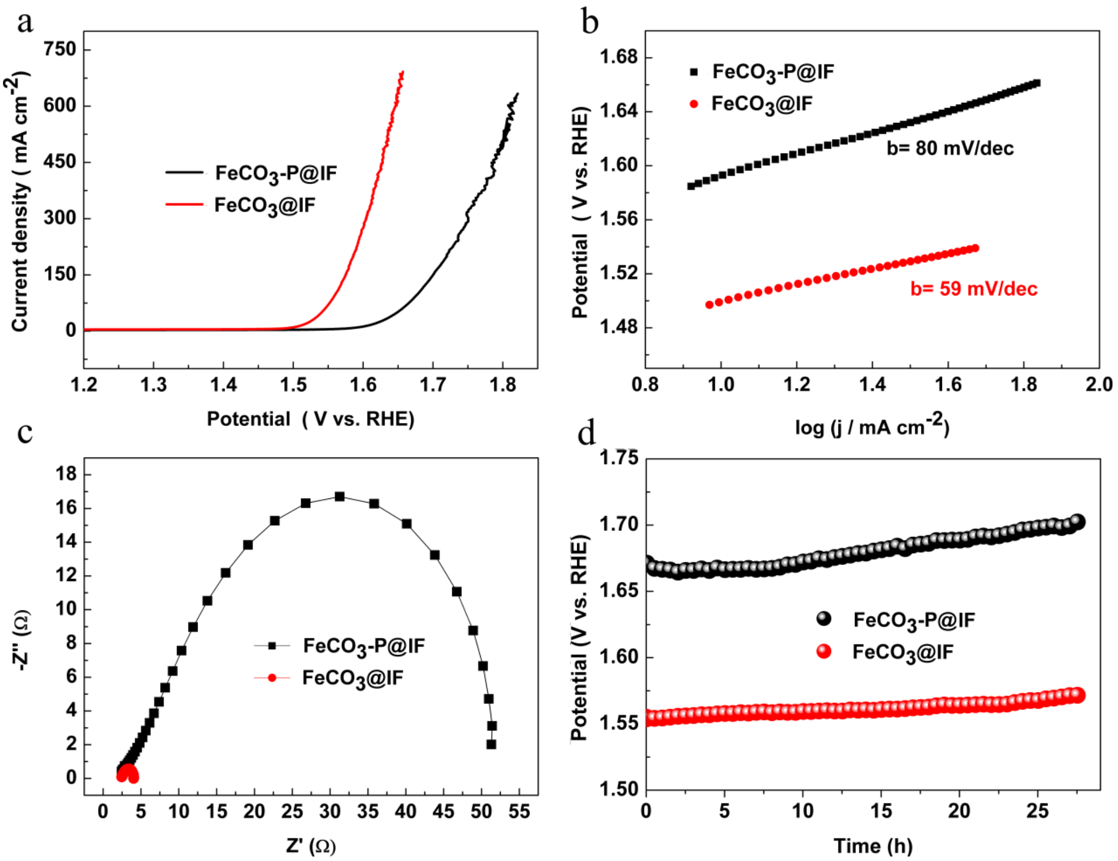

Fig. S11 a) the polarization curves, b) the Tafel plots, c) the EIS at 1.55 V vs. RHE and d) the stability test of the catalysts at the current density of 100 mA cm^{-2} for $FeCO_3$-P@IF and $FeCO_3$@IF, respectively.

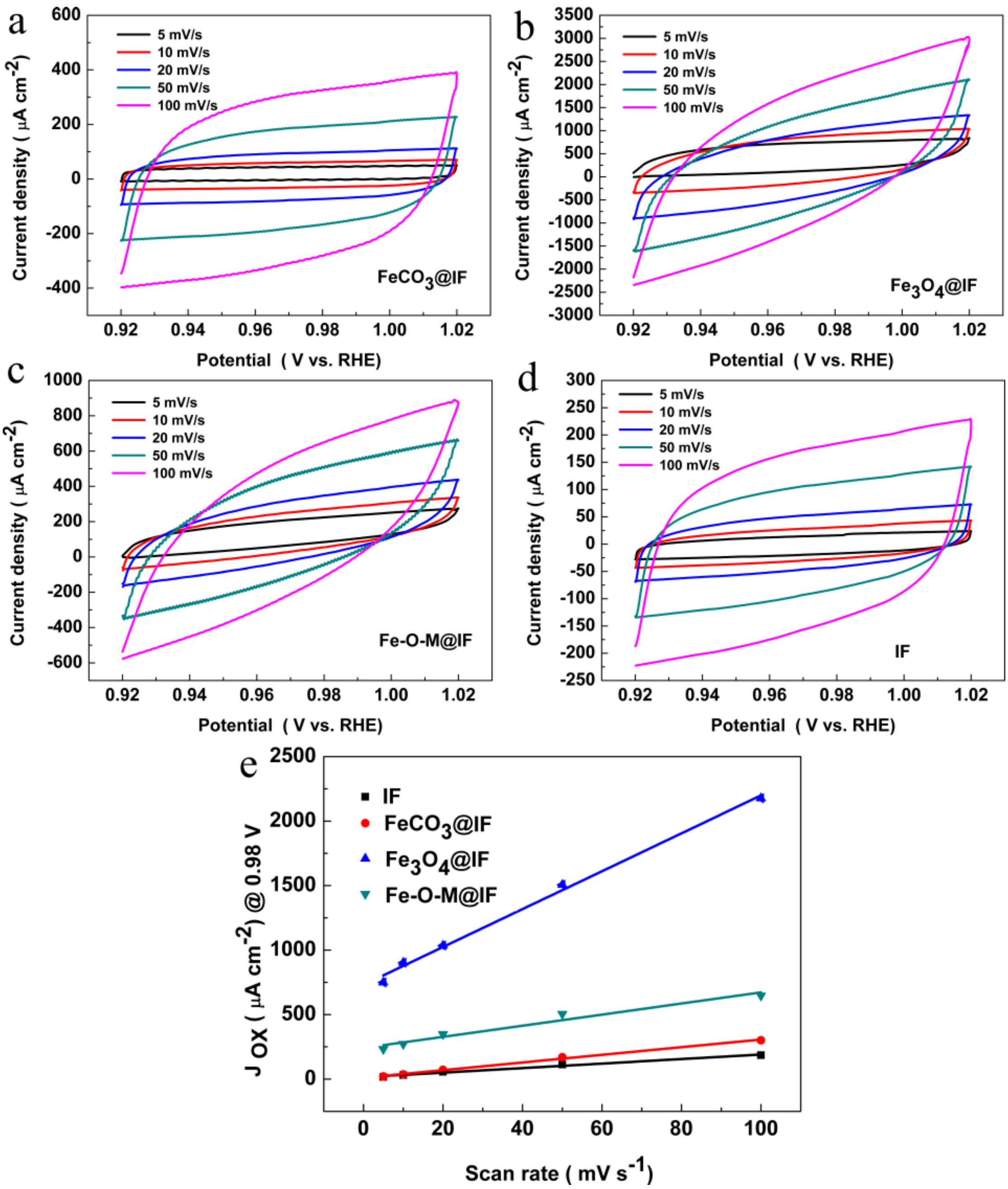

Fig. S12 The double-layer capacitance measurements of these catalysts after OER; a-d) the cyclic voltammograms of the catalysts at a series of scan rates of 5, 10, 20, 50 and 100 mV s^{-1} from 0.92 to 1.02 V vs. RHE in 1 M KOH; e) the linear fitting of the oxidation currents of the catalysts at 0.98 V vs. RHE versus scan rates.

Electrical double-layer capacitance measurements were used to determine electrochemical active surface area of the catalysts. According to Fig. S11e, the electrical double-layer capacitance could be obtained. Then the electrochemical active surface area could be obtained based on the specific capacitance value of a smooth standard with a real surface area of 1 cm^{-2}. 40 uF cm^{-2} is considered as the value of specific capacitance for a smooth standard with a real surface area of 1 cm^{-2} based on previous studies.

The electrochemical active surface area could be obtained via the following equation:

$$A_{ECSA}=\frac{\text{The electrical double-layer capacitor}}{40}$$

For example:

$$FeCO_3@IF: A_{ECSA} = \frac{2956.7}{40} = 73.9\ cm^2_{ECSA}$$

Table S5. The calculated electrochemical active surface area (ECSA) of the obtained electrodes after OER.

Catalysts	IF	$FeCO_3$@IF	Fe_3O_4@IF	Fe-O-M@IF
Specific Capacitance (uF cm^{-2})	1745.3	2956.7	14685.9	4309.6
ECSA (cm^2_{ECSA})	43.6	73.9	367.1	107.7

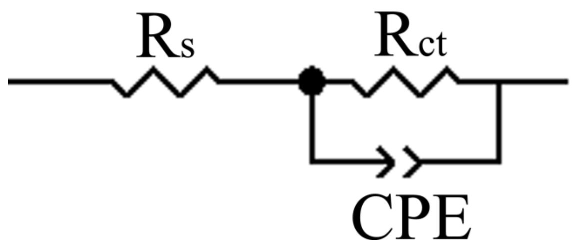

Fig. S13 The simplified randles equivalent circuit for the test of the electrochemical impedance spectroscopy.

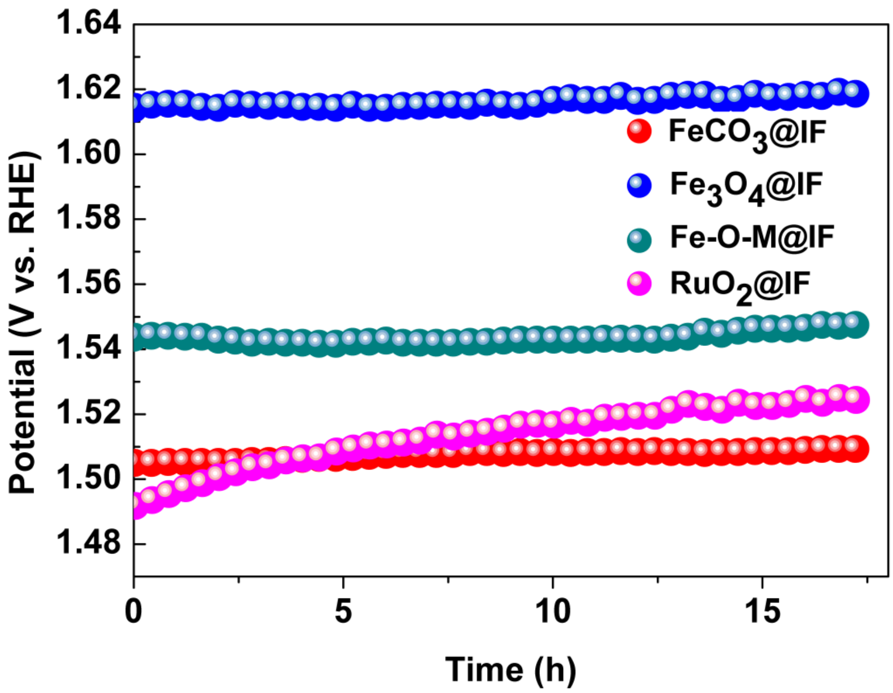

Fig. S14 The stability tests of the catalysts at the current density of 10 mA cm^{-2}.

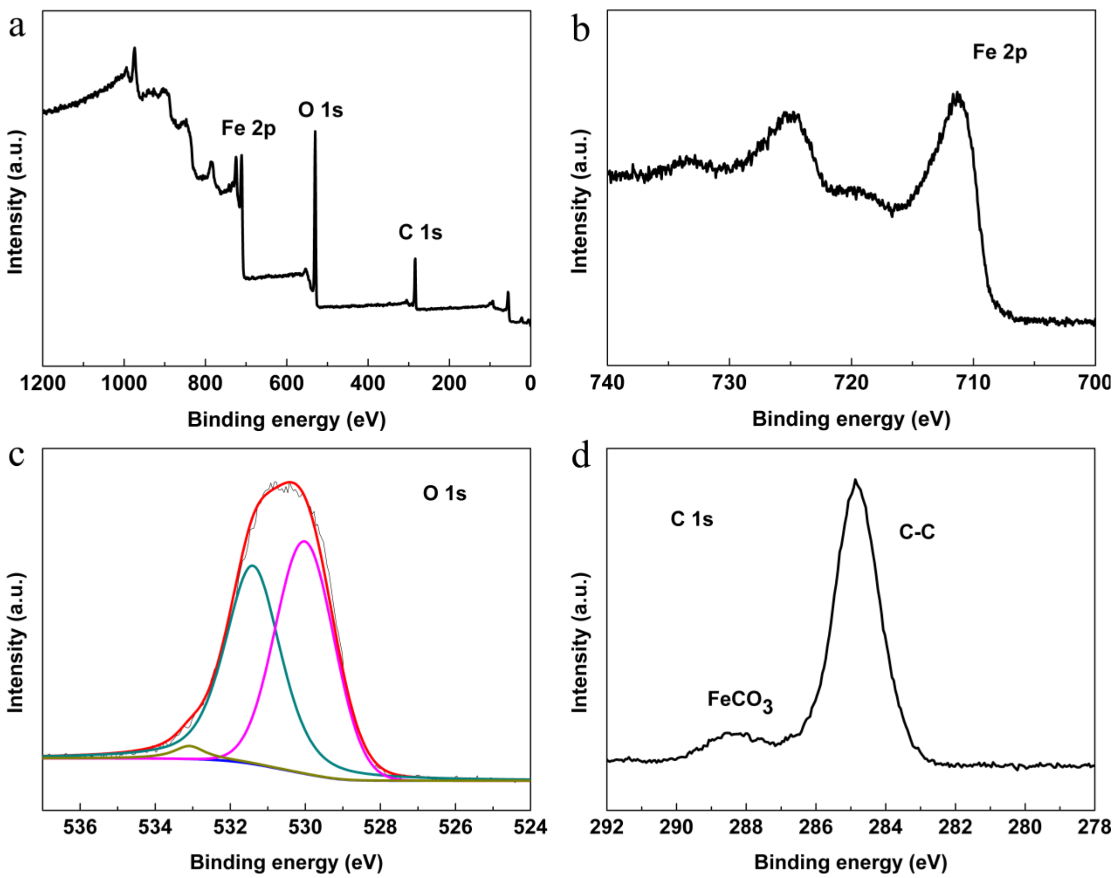

Fig. S15 a) The full XPS spectrum, b) Fe 2p, c) O 1s and d) C 1s of $FeCO_3$@IF after OER.

Table S6. According to the XPS spectra, the change of Fe content in different chemical environment for $FeCO_3$@IF before and after OER process.

$FeCO_3$@IF	Fe (%)		
Chemical environment	Fe (0)	Fe (2+)	Fe (3+)
Before OER	6.81	33.24	55.95
After OER	0	27.39	72.61

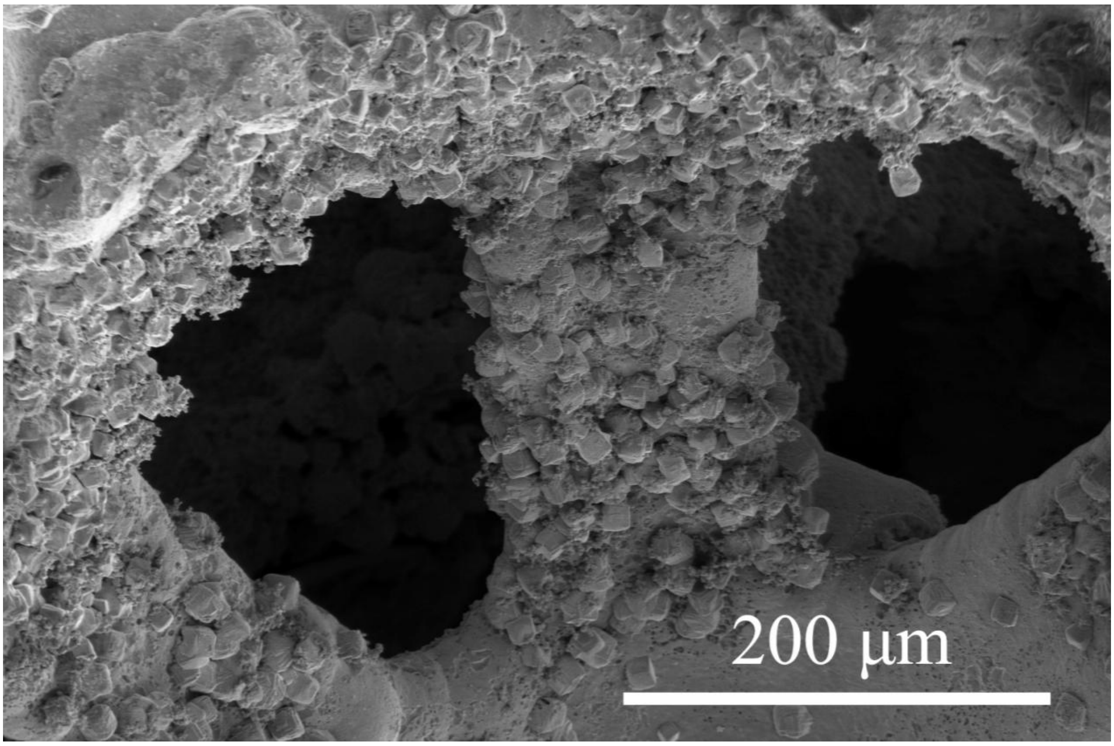

Fig. S16 The SEM image of $FeCO_3$@IF after OER.

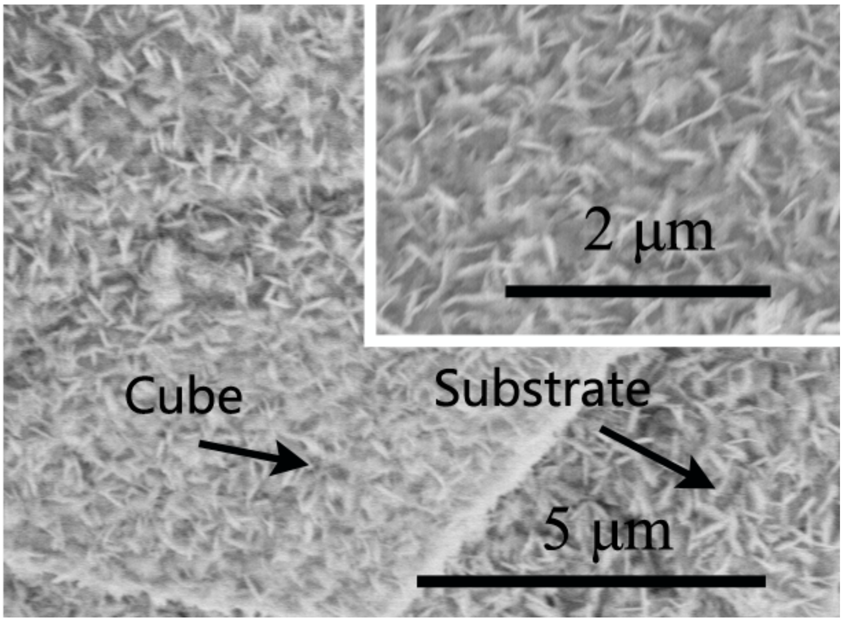

Fig. S17 The SEM image of the surface of $FeCO_3$ cube and the area without $FeCO_3$ cubes.

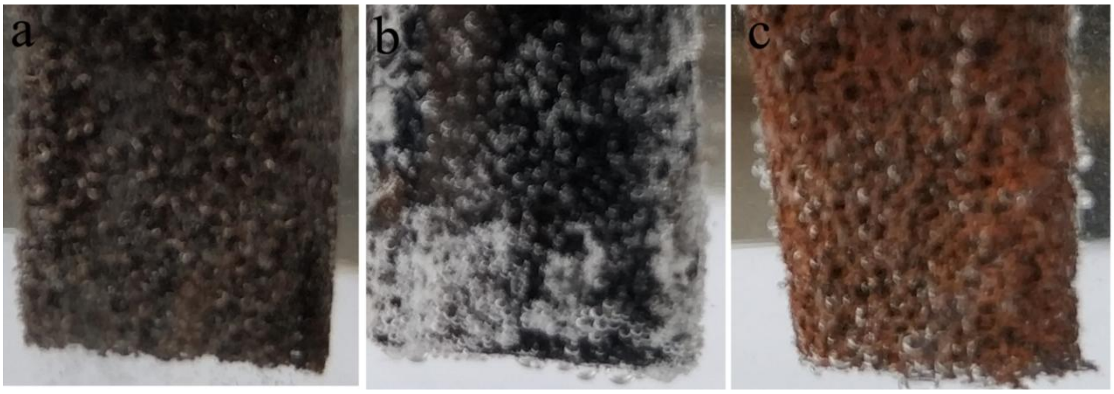

Fig. S18 The images of bubbles on the surface a) $FeCO_3$@IF, b)Fe_3O_4@IF and c) Fe-O-M@IF during OER process at the current density of 100 mA cm^{-2}.

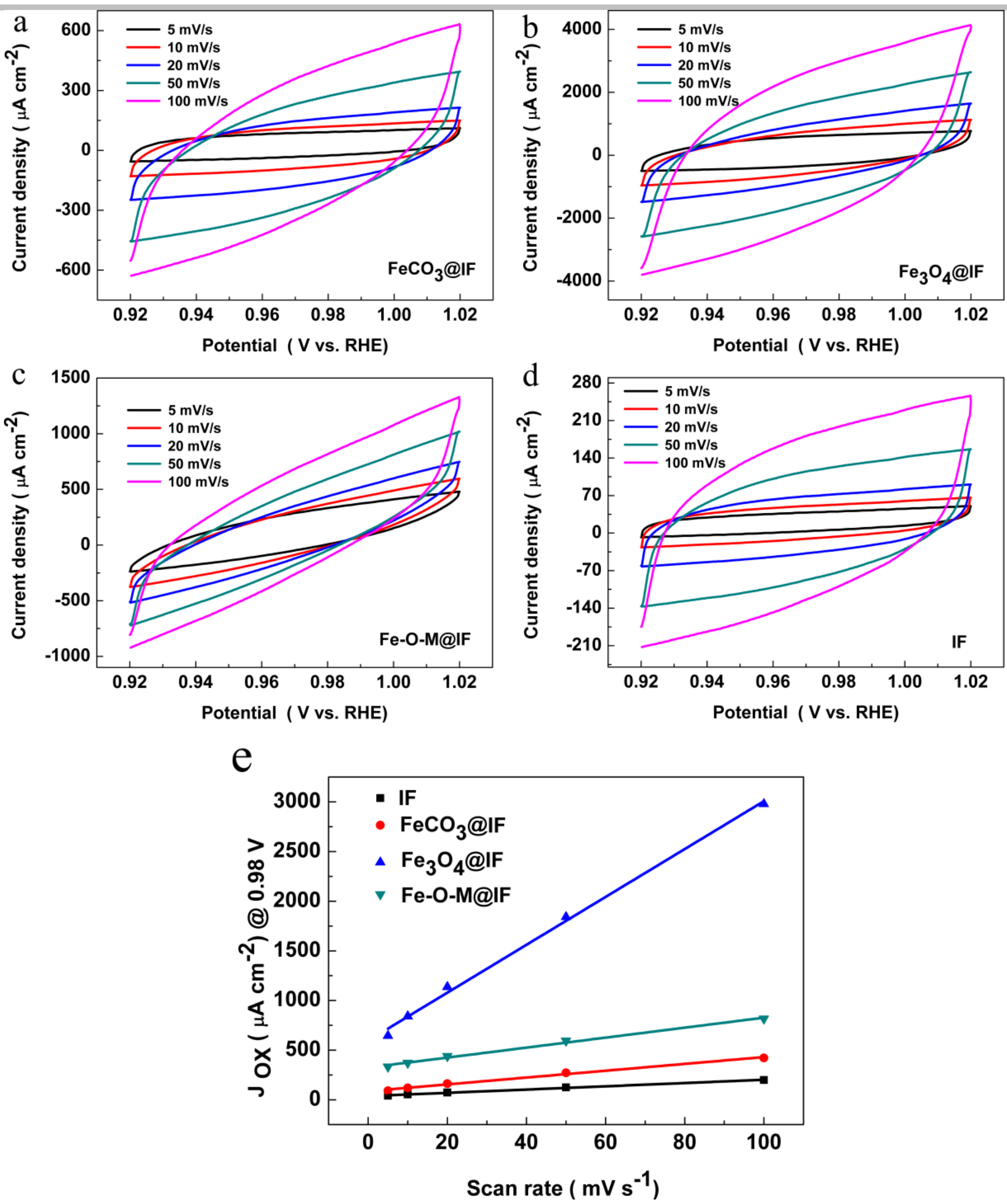

Fig. S19 The double-layer capacitance measurements of these catalysts after HER; a-d) the cyclic voltammograms of the catalysts at a series of scan rates of 5, 10, 20, 50 and 100 mV s^{-1} from 0.92 to 1.02 V vs. RHE in 1 M KOH; e) the linear fitting of the oxidation currents of the catalysts at 0.98 V vs. RHE versus scan rates.

Table S7. The calculated electrochemical active surface area (ECSA) of the obtained catalysts after HER.

Catalysts	IF	$FeCO_3$@IF	Fe_3O_4@IF	Fe-O-M@IF
Specific capacitance (uF cm^{-2})	1644.1	3436.8	24106.5	5023.5
ECSA (cm^2_{ECSA})	41.1	85.9	602.6	125.6

Table S8. The comparison of HER catalytic activity in 1 M KOH

Catalysts	Tafel slope (mV dec $^{-1}$)	Overpotential (mV) @ 10 mA cm $^{-2}$	References
Fe_2Ni_2N	101	180	[27]
CoS_2 HNSs	100	193	[28]
FeP NAs/CC	146	218	[29]
FeP/C	93	185	[30]
A-Ni@DG	47	270	[31]
Fe_2O_3	140	423	[32]
N-rGO/CoFe-$CoFe_2O_4$	100	190	[33]
Fe_2O_3NCs-800	77	245	[34]
FeCoO-NF	118	205	[35]
Co_9S_8@NOSC	105	320	[36]
Co_9S_8/Ni_3S_2	98	128	[37]
Ni_3FeN	120	235	[38]
$Ni_{2/3}Fe_{1/3}$-rGO	210	560	[39]
Ni@NC-800	160	205	[40]
CoNiP@Ti	115	184	[41]
$FeCO_3$@IF	139	151	This work

Table S9. The comparison of HER catalytic activity of the Pt/C (20%) in 1 M KOH

Catalysts	Tafel slope (mV dec $^{-1}$)	Overpotential (mV)@10 mA cm^{-2} /100 mA cm $^{-2}$	References
Pt/C@Iron foam	48	34/113	This work
Pt/C@Iron foam	37	～30/-	[15]
Pt/C@ Ni foam	56	～40/～165	[42]
Pt/C@Ni foam	45	～40/～150	[43]
Pt/C@Ni foam	37	～70/～210	[44]
Pt/C@Ni foam	49	27/～100	[18]
Pt/C@Ni foam	30	37/138	[17]
Pt/C@Ni foam	59	～50/～170	[45]
Pt/C@ Carbon cloth	48	～30/200	[46]
Pt/C@Carbon cloth	52	52/～290	[47]
Pt/C@Carbon paper	44	45/～120	[48]
Pt/C@ Glassy carbon	46	60/～135	[49]
Pt/C@Glassy carbon	37	27/109	[50]
Pt/C@Co foam	45	40/～100	[26]

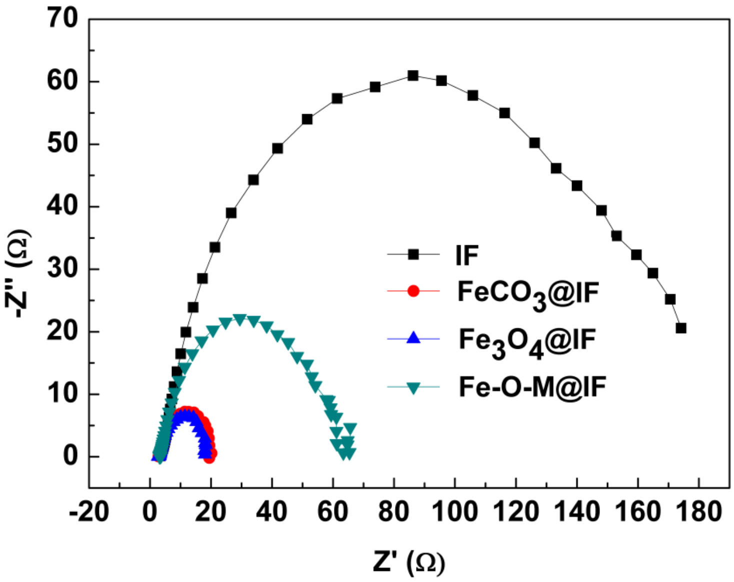

Fig. S20 The EIS of the catalytic eletrodes at -0.18 V vs. RHE

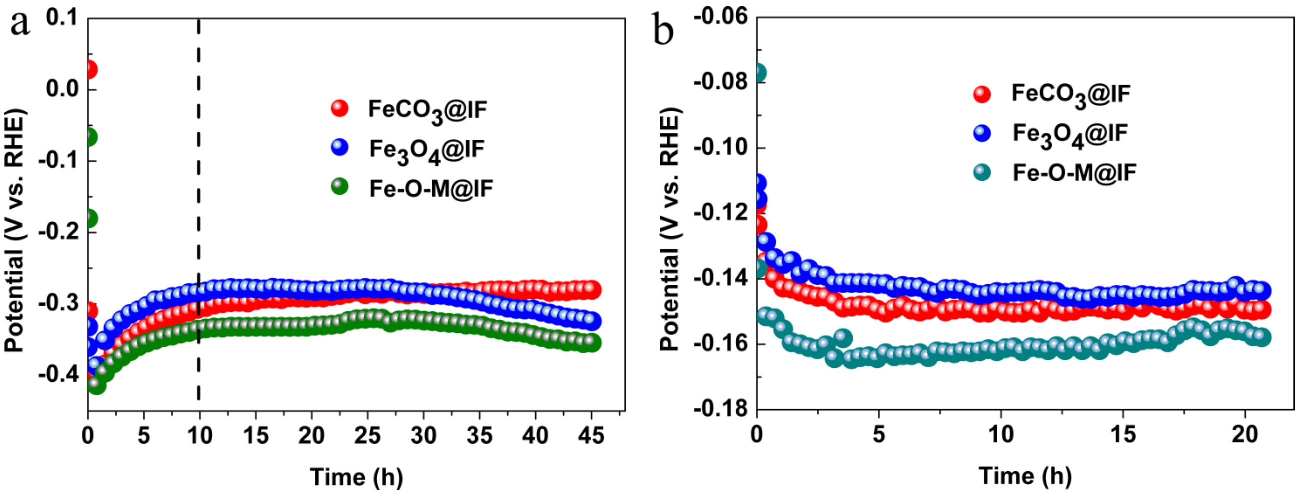

Fig. S21 The stability test of the catalysts at the current density of a) -100 mA cm^{-2} and b) -10 mA cm^{-2}.

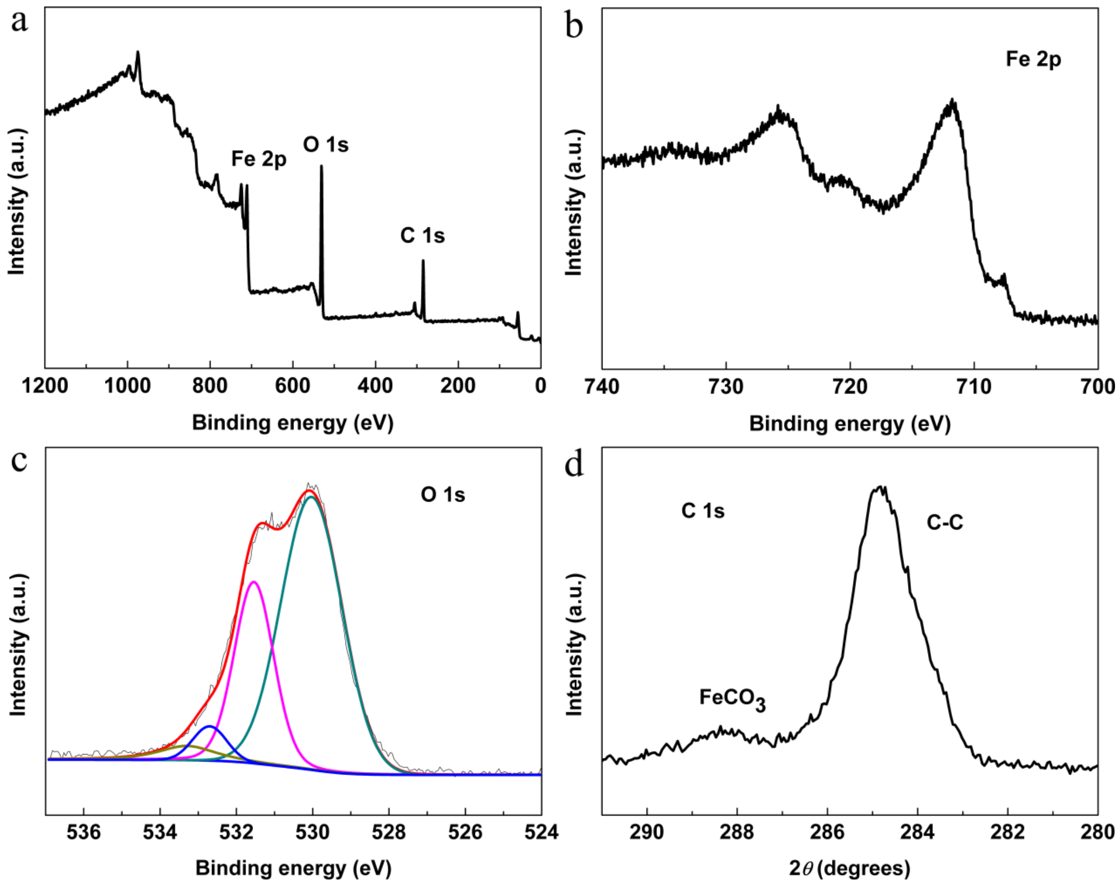

Fig. S22 a) The full XPS spectrum, b) Fe 2p, c) O 1s and d) C 1s of $FeCO_3$@IF after HER.

Table S10. According to the XPS spectra, the change of Fe content in different chemical environment for $FeCO_3$@IF before and after HER process.

$FeCO_3$@IF	Fe(%)		
Chemical environment	Fe (0)	Fe (2+)	Fe (3+)
Before HER	6.81	33.24	55.95
After HER	10.05	12.96	76.99

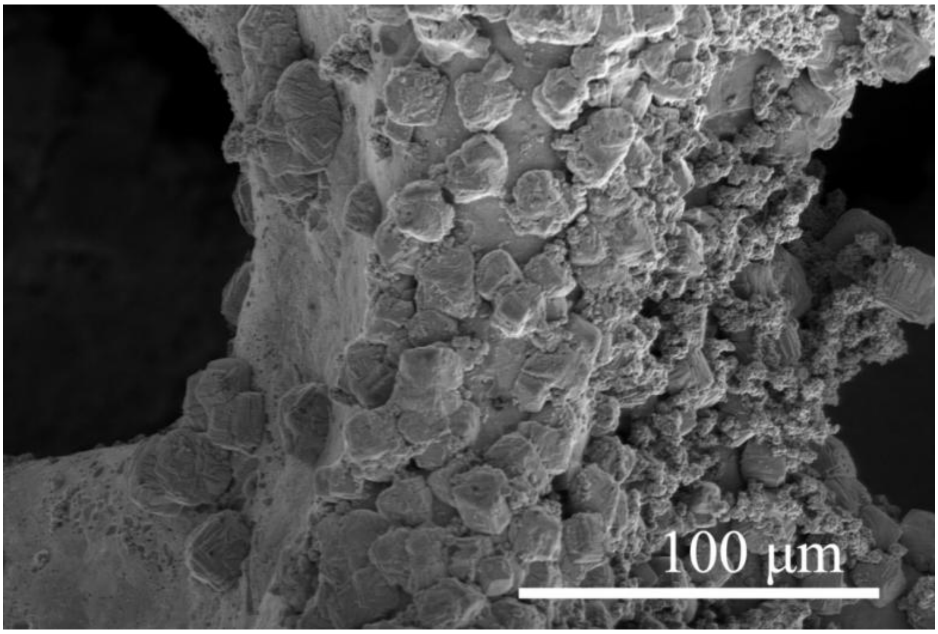

Fig. S23 The SEM image of $FeCO_3$@IF after HER.

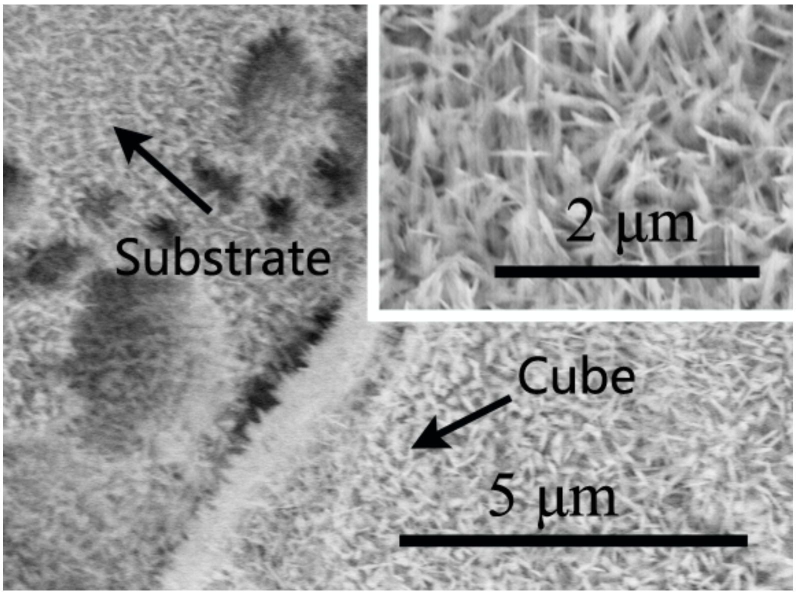

Fig. S24 The SEM image of the surface of $FeCO_3$ cube and the area without $FeCO_3$ cubes (the inset) of $FeCO_3$@IF after HER progress.

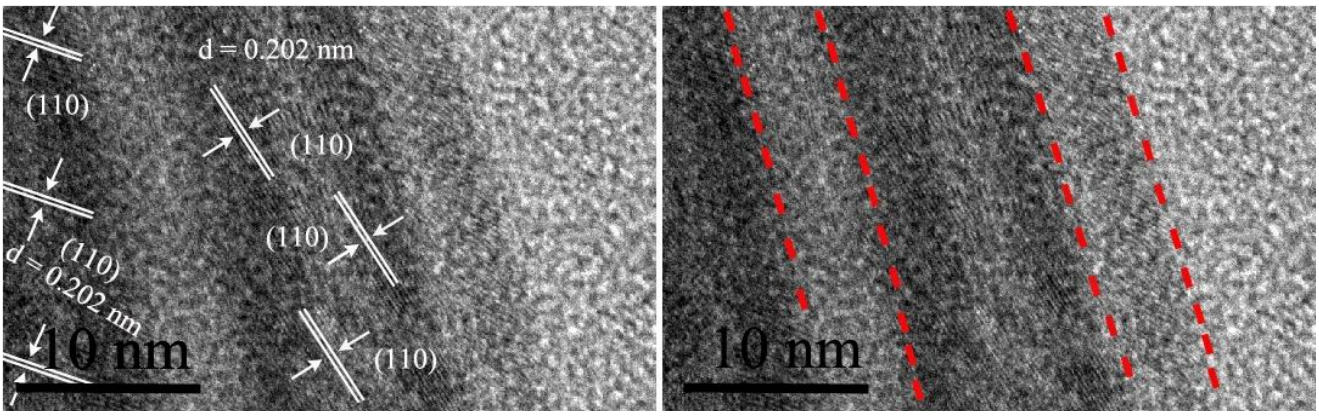

Fig. S25 The HTEM images of $FeCO_3$@IF after HER.

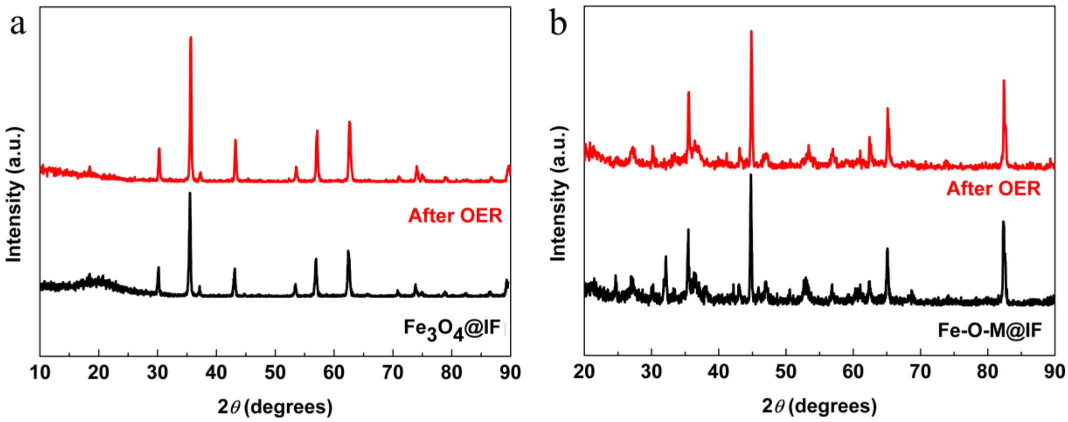

Fig. S26 The XRD patterns of a) Fe_3O_4@IF and b) Fe-O-M@IF before and after OER, respectively.

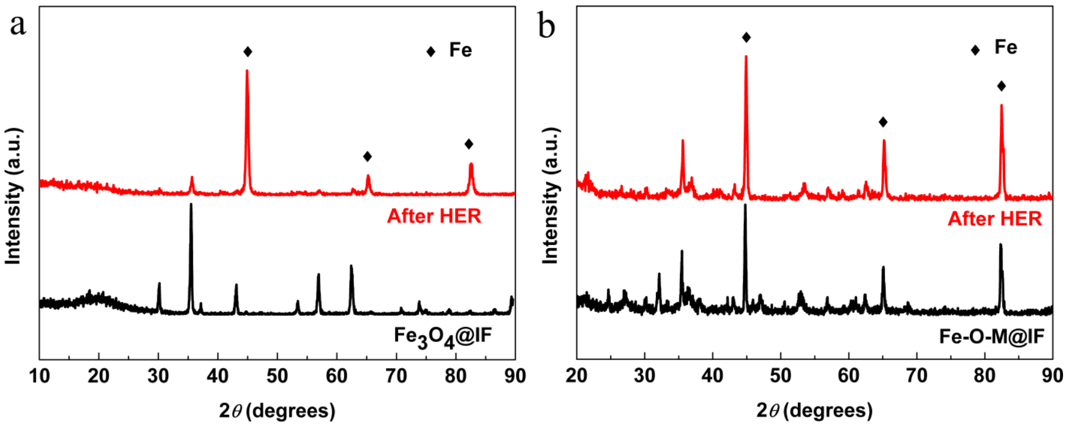

Fig. S27 The XRD patterns of a) Fe_3O_4@IF and b) Fe-O-M@IF before and after HER, respectively..

The peaks related to metallic iron all become stronger in the XRD patterns of Fe_3O_4@IF and Fe-O-M@IF after HER, indicating the iron-based compounds are reduced to metallic iron.

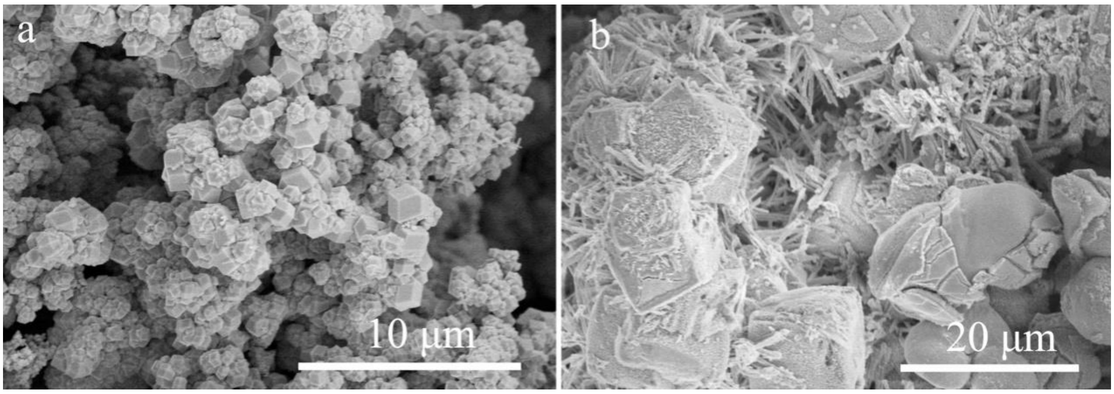

Fig. S28 The SEM images of a) Fe_3O_4@IF and b) Fe-O-M@IF after OER, respectively.

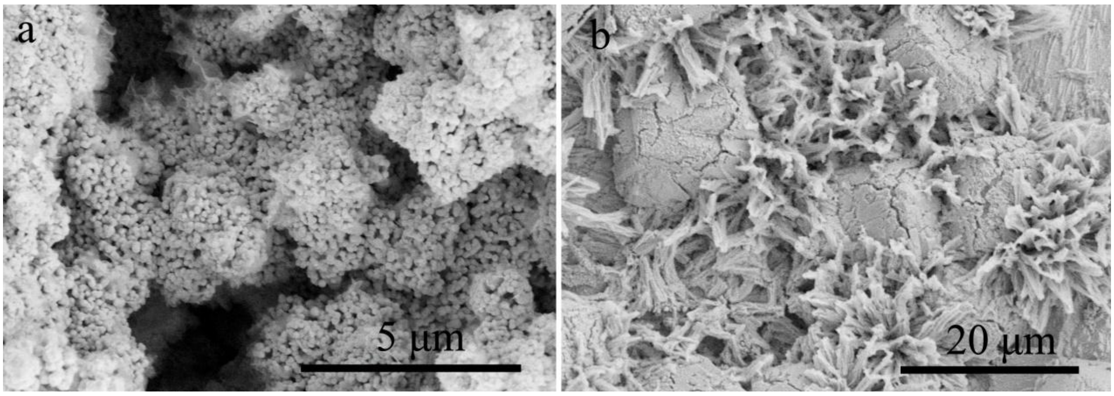

Fig. S29 The SEM images of a) Fe_3O_4@IF and b) Fe-O-M@IF after HER, respectively.

The particles on Fe-O-M@IF after HER become looser due to the loss of abundant O in iron-based oxides

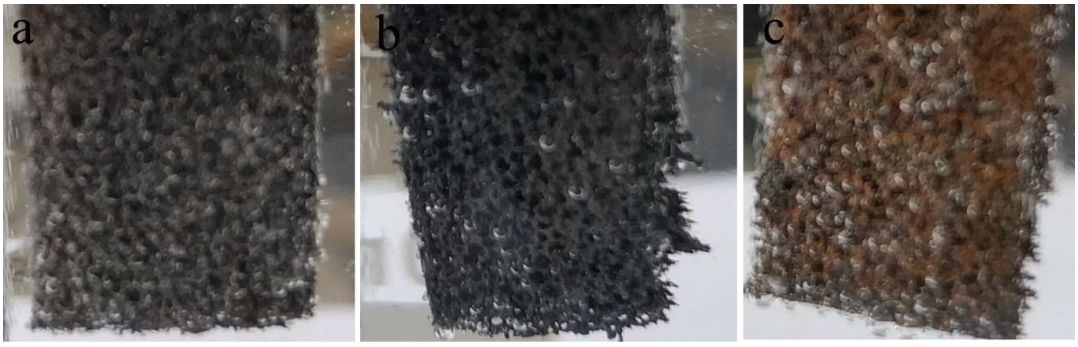

Fig. S30 The images of bubbles on the surface a) $FeCO_3$@IF, b)Fe_3O_4@IF and c) Fe-O-M@IF during HER process at the current density of 100 mA cm^{-2}

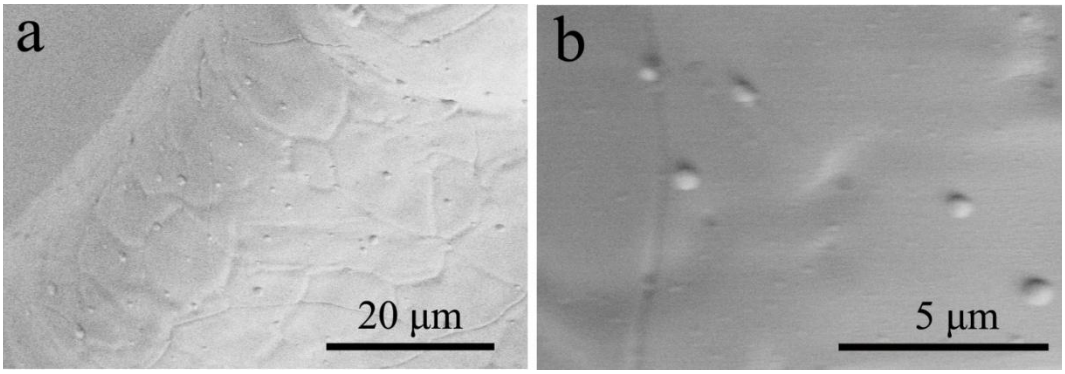

Fig. S31 The SEM images of IF electrode after OER.

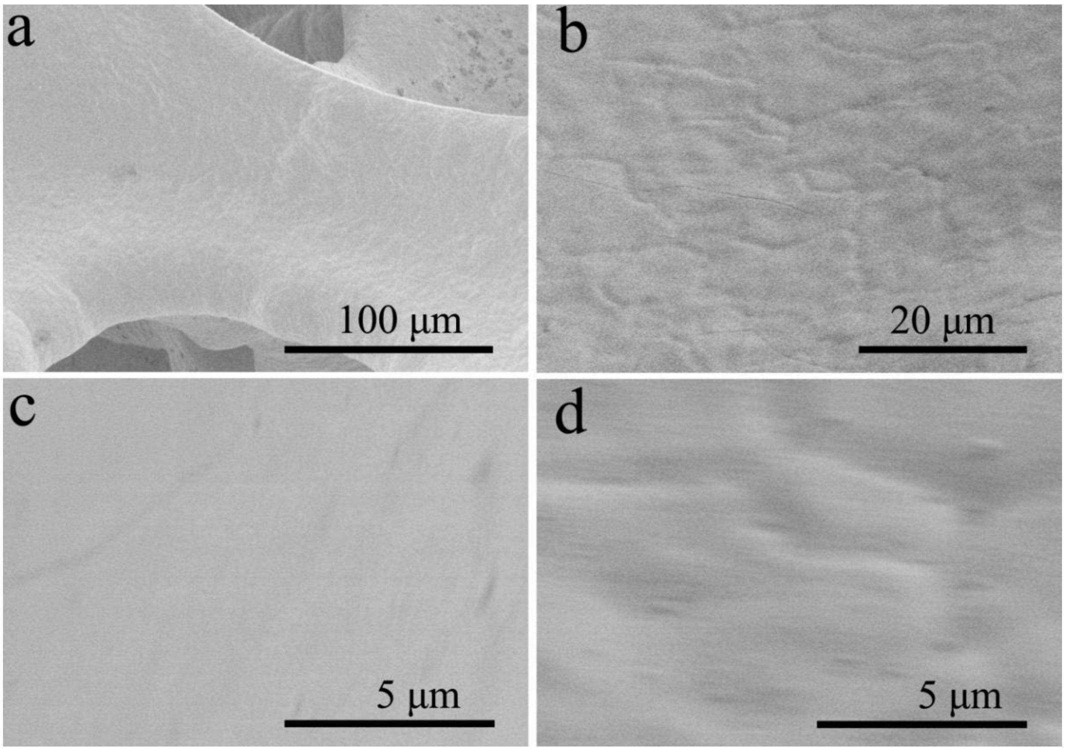

Fig. S32 The SEM images of IF after HER process.

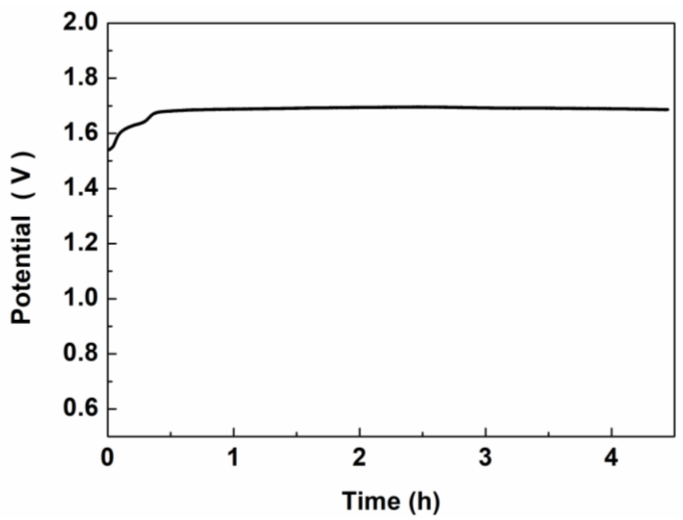

Fig. S33 The stability test of the $FeCO_3$@IF//$FeCO_3$@IF at the current density of 10 mA cm^{-2}.

Table S11. The comparison of overall water-splitting catalytic activity of the RuO_2//Pt/C system in 1 M KOH

Catalysts	Voltage (V) @ 50 mA cm^{-2}/100 mA cm^{-2}	References
RuO_2@Iron foam//Pt/C@Iron foam	1.697/1.863	This work
RuO_2@Iron foam //Pt/C@Iron foam	～1.74/-	[15]
RuO_2@Iron foam //Pt/C@Iron foam	～1.98/～2.24	[16]
RuO_2@Ni foam //Pt/C@Ni foam	1.770/-	[51]
RuO_2@Ni foam //Pt/C@Ni foam	～1.680/～1.770	[19]
RuO_2@Ni foam //Pt/C@Ni foam	～1.91/-	[18]
RuO_2@Glassy carbon//Pt/C@Glassy carbon	～1.800/～1.950	[49]
RuO_2@Carbon cloth//Pt/C@Carbon cloth	～1.650/-	[52]
RuO_2@Co foam //Pt/C@Co foam	1.780/～1.930	[26]

Table S12. The amount of electricity required to obtain 1 Kg H_2 of different electrodes in 1 M KOH

Catalytic electrodes	Voltage (V) @ 300 mA cm $^{-2}$/400 mA cm $^{-2}$	The amount of electricity (KW·h) @ 300 mA cm $^{-2}$/400 mA cm $^{-2}$
$FeCO_3$@IF//$FeCO_3$@IF	2.359/2.512	62.714/66.782
RuO_2@IF//Pt/C@IF	2.366/2.581	62.901/68.616

The calculation formula is as following:

1 Kg H_2 is generated, the required amount of charge (Q) is:

$$Q=(1000g\times N_A\times 2e)/M_{H_2}=(1000\times 2\times 6.022\times 10^{23}\times 1.602\times 10^{-19})/2.016=95706785.7\ C$$

Where N_A is Avogadro constant, e is the charge of an electron and M_{H2} is the relative molecular mass of hydrogen (H_2).

For the $FeCO_3$@IF//$FeCO_3$@IF system, the applied voltages (U1 and U2) at a current density of 300 mA cm^{-2} and 400 mA cm^{-2} is 2.359 V and 2.512 V, respectively. The amount of electricity (W1 and W2) required to obtain 1 Kg H_2 are:

$$W1 = QU1 = 95706785.7\times 2.359 = 225772307.466\ J \approx 62.714\ KW\cdot h$$

$$W2 = QU2 = 95706785.7\times 2.512 = 240415445.678\ J \approx 66.782\ KW\cdot h$$

For RuO_2@IF//Pt/C@IF system, the applied voltages (U3 and U4) at the current density of 300 mA cm^{-2} and 400 mA cm^{-2} is 2.366 V and 2.581 V, respectively.

The amount of electricity (W3 and W4) required to obtain 1 Kg H_2 are:

$$W3 = QU3 = 95706785.7\times 2.366 = 226442254.966\ J \approx 62.901\ KW\cdot h$$

$$W4 = QU4 = 95706785.7\times 2.581 = 247019213.892\ J \approx 68.616\ KW\cdot h$$

Therefore, the saved energy ($W1_{save}$ and $W2_{save}$) at the current density of 300 mA cm^{-2} and 400 mA cm^{-2} per kilogram H_2 are:

$$W1_{save} = W3 - W1 = 62.901 - 62.714 = 0.187\ KW\cdot h$$

$$W2_{save} = W4 - W2 = 68.616 - 66.782 = 1.834\ KW\cdot h$$

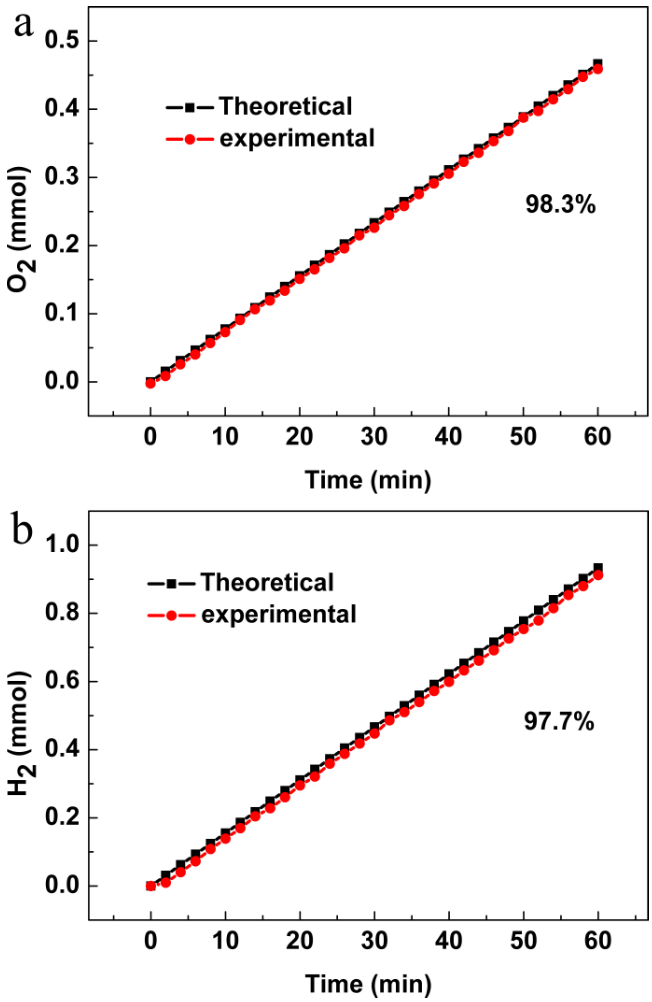

Fig. S34 The faladaic efficiency a) OER, b)HER) of the $FeCO_3$@IF at the current density of 50 mA cm^{-2}.

References

[1] F. Yan, C. Zhu, S. Wang, Y. Zhao, X. Zhang, C. Li, Y. Chen, Electrochemically activated-iron oxide nanosheet arrays on carbon fiber cloth as a three-dimensional self-supported electrode for efficient water oxidation, Journal of Materials Chemistry A, 4 (2016) 6048-6055.

[2] J. Lee, H. Lee, B. Lim, Chemical transformation of iron alkoxide nanosheets to FeOOH nanoparticles for highly active and stable oxygen evolution electrocatalysts, Journal of Industrial and Engineering Chemistry, 58 (2018) 100-104.

[3] Y. Shao, M. Zheng, M. Cai, L. He, C. Xu, Improved Electrocatalytic Performance of Core-shell NiCo/$NiCoO_x$ with amorphous FeOOH for Oxygen-evolution Reaction, Electrochimica Acta, 257 (2017) 1-8.

[4] H.A. Bandal, A.R. Jadhav, A.A. Chaugule, W.J. Chung, H. Kim, Fe_2O_3 hollow nanorods/CNT composites as an efficient electrocatalyst for oxygen evolution reaction, Electrochimica Acta, 222 (2016) 1316-1325.

[5] D. Xiong, X. Wang, W. Li, L. Liu, Facile synthesis of iron phosphide nanorods for efficient and durable electrochemical oxygen evolution, Chemical Communications, 52 (2016) 8711-8714.

[6] T. Gao, C. Zhou, Y. Zhang, Z. Jin, H. Yuan, D. Xiao, Ultra-fast pyrolysis of ferrocene to form Fe/C heterostructures as robust oxygen evolution electrocatalysts, Journal of Materials Chemistry A, 6 (2018) 21577-21584.

[7] P. Chen, K. Xu, Z. Fang, Y. Tong, J. Wu, X. Lu, X. Peng, H. Ding, C. Wu, Y. Xie, Metallic Co4N Porous Nanowire Arrays Activated by Surface Oxidation as Electrocatalysts for the Oxygen Evolution Reaction, Angewandte Chemie International Edition, 54 (2015) 14710-14714.

[8] Y. Tan, H. Wang, P. Liu, Y. Shen, C. Cheng, A. Hirata, T. Fujita, Z. Tang, M. Chen, Versatile nanoporous bimetallic phosphides towards electrochemical water splitting, Energy & Environmental Science, 9 (2016) 2257-2261.

[9] H. Liang, F. Meng, M. Cabán-Acevedo, L. Li, A. Forticaux, L. Xiu, Z. Wang, S. Jin, Hydrothermal Continuous Flow Synthesis and Exfoliation of NiCo Layered Double Hydroxide Nanosheets for Enhanced Oxygen Evolution Catalysis, Nano Letters, 15 (2015) 1421-1427.

[10] K. Yan, T. Lafleur, J. Chai, C. Jarvis, Facile synthesis of thin NiFe-layered double hydroxides nanosheets efficient for oxygen evolution, Electrochemistry Communications, 62 (2016) 24-28.

[11] J.A. Haber, Y. Cai, S. Jung, C. Xiang, S. Mitrovic, J. Jin, A.T. Bell, J.M. Gregoire, Discovering Ce-rich oxygen evolution catalysts, from high throughput screening to water electrolysis, Energy & Environmental Science, 7 (2014) 682-688.

[12] T. Gao, Z. Jin, Y. Zhang, G. Tan, H. Yuan, D. Xiao, Coupling cobalt-iron bimetallic nitrides and N-doped multi-walled carbon nanotubes as high-performance bifunctional catalysts for oxygen evolution and reduction reaction, Electrochimica Acta, 258 (2017) 51-60.

[13] M. Shalom, D. Ressnig, X. Yang, G. Clavel, T.P. Fellinger, M. Antonietti, Nickel nitride as an efficient electrocatalyst for water splitting, Journal of Materials Chemistry A, 3 (2015) 8171-8177.

[14] H. Liang, A.N. Gandi, D.H. Anjum, X. Wang, U. Schwingenschlögl, H.N. Alshareef, Plasma-Assisted Synthesis of NiCoP for Efficient Overall Water Splitting, Nano Letters, 16 (2016) 7718-7725.

[15] G. Li, J. Yu, W. Yu, L. Yang, X. Zhang, X. Liu, H. Liu, W. Zhou, Phosphorus-Doped Iron Nitride Nanoparticles Encapsulated by Nitrogen-Doped Carbon Nanosheets on Iron Foam In Situ Derived from Saccharomycetes Cerevisiae for Electrocatalytic Overall Water Splitting, Small, (2020) 2001980.

[16] Y. Wang, B. Ma, Y. Chen, Iron phosphides supported on three-dimensional iron foam as an efficient electrocatalyst for water splitting reactions, Journal of Materials Science, 54 (2019) 14872-14883.

[17] Z. Zou, X. Wang, J. Huang, Z. Wu, F. Gao, An Fe-doped nickel selenide nanorod/nanosheet hierarchical array for efficient overall water splitting, Journal of Materials Chemistry A, 7 (2019) 2233-2241.

[18] Y. Li, F. Li, Y. Zhao, S. Li, J. Zeng, H. Yao, Y. Chen, Iron doped cobalt phosphide ultrathin nanosheets on nickel foam for overall water splitting, Journal of Materials Chemistry A, 7 (2019) 20658-20666.

[19] M. Qu, Y. Jiang, M. Yang, S. Liu, Q. Guo, W. Shen, M. Li, R. He, Regulating electron density of NiFe-P nanosheets electrocatalysts by a trifle of Ru for high-efficient overall water splitting, Applied Catalysis B: Environmental, 263 (2020) 118324.

[20] J. Guo, K. Zhang, Y. Sun, Q. Liu, L. Tang, X. Zhang, Efficient bifunctional vanadium-doped Ni3S2 nanorod array for overall water splitting, Inorganic Chemistry Frontiers, 6 (2019) 443-450.

[21] J. Lin, P. Wang, H. Wang, C. Li, X. Si, J. Qi, J. Cao, Z. Zhong, W. Fei, J. Feng, Defect-Rich Heterogeneous MoS_2/NiS_2 Nanosheets Electrocatalysts for Efficient Overall Water Splitting, 6 (2019) 1900246.

[22] S. Dutta, A. Indra, Y. Feng, H. Han, T. Song, Promoting electrocatalytic overall water splitting with nanohybrid of transition metal nitride-oxynitride, Applied Catalysis B: Environmental, 241 (2019) 521-527.

[23] J. Lin, Y. Yan, C. Li, X. Si, H. Wang, J. Qi, J. Cao, Z. Zhong, W. Fei, J. Feng, Bifunctional Electrocatalysts Based on Mo-Doped NiCoP Nanosheet Arrays for Overall Water Splitting, Nano-Micro Letters, 11 (2019) 55.

[24] G. Zhou, M. Li, Y. Li, H. Dong, D. Sun, X. Liu, L. Xu, Z. Tian, Y. Tang, Regulating the Electronic Structure of CoP Nanosheets by O Incorporation for High-Efficiency Electrochemical Overall Water Splitting, 30 (2020) 1905252.

[25] L. Ji, J. Wang, X. Teng, T. Meyer, Z. Chen, CoP Nanoframes as Bifunctional Electrocatalysts for Efficient Overall Water Splitting, ACS Catalysis, 10 (2020) 412-419.

[26] Z. Liu, X. Yu, H. Xue, L. Feng, A nitrogen-doped CoP nanoarray over 3D porous Co foam as an efficient bifunctional electrocatalyst for overall water splitting, Journal of Materials Chemistry A, 7 (2019) 13242-13248.

[27] M. Jiang, Y. Li, Z. Lu, X. Sun, X. Duan, Binary nickel-iron nitride nanoarrays as bifunctional electrocatalysts for overall water splitting, Inorganic Chemistry Frontiers, 3 (2016) 630-634.
[28] X. Ma, W. Zhang, Y. Deng, C. Zhong, W. Hu, X. Han, Phase and composition controlled synthesis of cobalt sulfide hollow nanospheres for electrocatalytic water splitting, Nanoscale, 10 (2018) 4816-4824.
[29] Y. Liang, Q. Liu, A.M. Asiri, X. Sun, Y. Luo, Self-Supported FeP Nanorod Arrays: A Cost-Effective 3D Hydrogen Evolution Cathode with High Catalytic Activity, ACS Catalysis, 4 (2014) 4065-4069.
[30] F. Wang, X. Yang, B. Dong, X. Yu, H. Xue, L. Feng, A FeP powder electrocatalyst for the hydrogen evolution reaction, Electrochemistry Communications, 92 (2018) 33-38.
[31] L. Zhang, Y. Jia, G. Gao, X. Yan, N. Chen, J. Chen, M.T. Soo, B. Wood, D. Yang, A. Du, X. Yao, Graphene Defects Trap Atomic Ni Species for Hydrogen and Oxygen Evolution Reactions, Chem, 4 (2018) 285-297.
[32] R.N. Ali, H. Naz, X. Zhu, J. Xiang, G. Hu, B. Xiang, Synthesis, characterization and applications of pH controlled Fe_2O_3 nanoparticles for electrocatalytic hydrogen evolution reaction, Materials Research Express, 6 (2018) 025516.
[33] Z. Wu, P. Li, Q. Qin, Z. Li, X. Liu, N-doped graphene combined with alloys (NiCo, CoFe) and their oxides as multifunctional electrocatalysts for oxygen and hydrogen electrode reactions, Carbon, 139 (2018) 35-44.
[34] J. Jiang, L. Zhu, Y. Sun, Y. Chen, H. Chen, S. Han, H. Lin, Fe_2O_3 nanocatalysts on N-doped carbon nanomaterial for highly efficient electrochemical hydrogen evolution in alkaline, Journal of Power Sources, 426 (2019) 74-83.
[35] H.A. Bandal, A.R. Jadhav, A.H. Tamboli, H. Kim, Bimetallic iron cobalt oxide self-supported on Ni-Foam: An efficient bifunctional electrocatalyst for oxygen and hydrogen evolution reaction, Electrochimica Acta, 249 (2017) 253-262.
[36] S. Huang, Y. Meng, S. He, A. Goswami, Q. Wu, J. Li, S. Tong, T. Asefa, M. Wu, N-, O-, and S-Tridoped Carbon-Encapsulated Co_9S_8 Nanomaterials: Efficient Bifunctional Electrocatalysts for Overall Water Splitting, Advanced Functional Materials, 27 (2017) 1606585.
[37] F. Du, L. Shi, Y. Zhang, T. Li, J. Wang, G. Wen, A. Alsaedi, T. Hayat, Y. Zhou, Z. Zou, Foam-like Co_9S_8/Ni_3S_2 heterostructure nanowire arrays for efficient bifunctional overall water-splitting, Applied Catalysis B: Environmental, 253 (2019) 246-252.
[38] Y. Gu, S. Chen, J. Ren, Y.A. Jia, C. Chen, S. Komarneni, D. Yang, X. Yao, Electronic Structure Tuning in Ni_3FeN/r-GO Aerogel toward Bifunctional Electrocatalyst for Overall Water Splitting, ACS Nano, 12 (2018) 245-253.
[39] W. Ma, R. Ma, C. Wang, J. Liang, X. Liu, K. Zhou, T. Sasaki, A Superlattice of Alternately Stacked Ni-Fe Hydroxide Nanosheets and Graphene for Efficient Splitting of Water, ACS Nano, 9 (2015) 1977-1984.
[40] Y. Xu, W. Tu, B. Zhang, S. Yin, Y. Huang, M. Kraft, R. Xu, Nickel Nanoparticles Encapsulated in Few-Layer Nitrogen-Doped Graphene Derived from Metal-Organic Frameworks as Efficient Bifunctional Electrocatalysts for Overall Water Splitting, Advanced Materials, 29 (2017) 1605957.
[41] A. Han, H. Chen, H. Zhang, Z. Sun, P. Du, Ternary metal phosphide nanosheets as a highly efficient electrocatalyst for water reduction to hydrogen over a wide pH range from 0 to 14, Journal of Materials Chemistry A, 4 (2016) 10195-10202.
[42] Y. Yang, K. Zhang, H. Lin, X. Li, H.C. Chan, L. Yang, Q. Gao, MoS_2-Ni_3S_2 Heteronanorods as Efficient and Stable Bifunctional Electrocatalysts for Overall Water Splitting, ACS Catalysis, 7 (2017) 2357-2366.
[43] P. Wang, Z. Pu, W. Li, J. Zhu, C. Zhang, Y. Zhao, S. Mu, Coupling $NiSe_2$-Ni_2P heterostructure nanowrinkles for highly efficient overall water splitting, Journal of Catalysis, 377 (2019) 600-608.
[44] W. Ye, Y. Yang, X. Fang, M. Arif, X. Chen, D. Yan, 2D Cocrystallized Metal-Organic Nanosheet Array as an Efficient and Stable Bifunctional Electrocatalyst for Overall Water Splitting, ACS Sustainable Chemistry & Engineering, 7 (2019) 18085-18092.
[45] Y. Xiong, L. Xu, C. Jin, Q. Sun, Interface-engineered atomically thin Ni_3S_2/MnO_2 heterogeneous nanoarrays for efficient overall water splitting in alkaline media, Applied Catalysis B: Environmental, 254 (2019) 329-338.
[46] C. Guan, W. Xiao, H. Wu, X. Liu, W. Zang, H. Zhang, J. Ding, Y.P. Feng, S.J. Pennycook, J. Wang, Hollow Mo-doped CoP nanoarrays for efficient overall water splitting, Nano Energy, 48 (2018) 73-80.
[47] Z. Chen, Y. Ha, H. Jia, X. Yan, M. Chen, M. Liu, R. Wu, Oriented Transformation of Co-LDH into 2D/3D ZIF-67 to Achieve Co-N-C Hybrids for Efficient Overall Water Splitting, 9 (2019) 1803918.
[48] L. Dai, Z. Chen, L. Li, P. Yin, Z. Liu, H. Zhang, Ultrathin Ni(0)-Embedded $Ni(OH)_2$ Heterostructured Nanosheets with Enhanced Electrochemical Overall Water Splitting, 32 (2020) 1906915.
[49] Z. Liu, M. Zha, Q. Wang, G. Hu, L. Feng, Overall water-splitting reaction efficiently catalyzed by a novel bi-functional Ru/Ni_3N-Ni electrode, Chemical Communications, 56 (2020) 2352-2355.
[50] C. Zhang, H. Liu, J. He, G. Hu, H. Bao, F. Lü, L. Zhuo, J. Ren, X. Liu, J. Luo, Boosting hydrogen evolution activity of vanadyl pyrophosphate nanosheets for electrocatalytic overall water splitting, Chemical Communications, 55 (2019) 10511-10514.
[51] H. Yan, Y. Xie, A. Wu, Z. Cai, L. Wang, C. Tian, X. Zhang, H. Fu, Anion-Modulated HER and OER Activities of 3D Ni-V-Based Interstitial Compound Heterojunctions for High-Efficiency and Stable Overall Water Splitting, 31 (2019) 1901174.
[52] J. Lin, P. Wang, H. Wang, C. Li, X. Si, J. Qi, J. Cao, Z. Zhong, W. Fei, J. Feng, Defect-Rich Heterogeneous MoS_2/NiS_2 Nanosheets Electrocatalysts for Efficient Overall Water Splitting, Advanced Science, 6 (2019) 1900246.